Combined fluorescence, optical diffraction tomography and Brillouin microscopy

Raimund Schlüßler[1,*,+], Kyoohyun Kim[1,2,,+], Martin Nötzel[1], Anna Taubenberger[1], Shada Abuhattum[1,2], Timon Beck[1,2], Paul Müller[1,2], Shovamayee Maharana[1], Gheorghe Cojoc[1], Salvatore Girardo[1,2], Andreas Hermann[3], Simon Alberti[1,4], and Jochen Guck[1,2,4,***]**

[1]Biotechnology Center, Center for Molecular and Cellular Bioengineering, Technische Universität Dresden, 01307 Dresden, Germany
[2]Max Planck Institute for the Science of Light and Max-Planck-Zentrum für Physik und Medizin, 91058 Erlangen, Germany
[3]Translational Neurodegeneration Section "Albrecht Kossel", University Rostock, and German Center for Neurodegenerative Diseases (DZNE), Rostock/Greifswald, 18147 Rostock, Germany
[4]Physics of Life, Technische Universität Dresden, 01307 Dresden, Germany
[*]raimund.schluessler@tu-dresden.de
[**]kyoohyun.kim@mpl.mpg.de
[***]jochen.guck@mpl.mpg.de
[+]these authors contributed equally to this work

ABSTRACT

Quantitative measurements of physical parameters become increasingly important for understanding biological processes. Brillouin microscopy (BM) has recently emerged as one technique providing the 3D distribution of viscoelastic properties inside biological samples — so far relying on the implicit assumption that refractive index (RI) and density can be neglected. Here, we present a novel method (FOB microscopy) combining BM with optical diffraction tomography and epi-fluorescence imaging for explicitly measuring the Brillouin shift, RI and absolute density with molecular specificity. We show that neglecting the RI and density might lead to erroneous conclusions. Investigating the cell nucleus, we find that it has lower density but higher longitudinal modulus. Thus, the longitudinal modulus is not merely sensitive to the water content of the sample — a postulate vividly discussed in the field. We demonstrate the further utility of FOB on various biological systems including adipocytes and intracellular membraneless compartments. FOB microscopy can provide unexpected scientific discoveries and shed quantitative light on processes such as phase separation and transition inside living cells.

Introduction

The mechanical properties of tissues, single cells, and intracellular compartments are linked to their function, in particular during migration and differentiation, and as a response to external stress[1–3]. Hence, characterizing mechanical properties *in vivo* has become important for understanding cell physiology and pathology, e.g. during development or cancer progression.[4–6] To measure the mechanical properties of biological samples, many techniques are available. These include atomic force microscopy[7–10], micropipette aspiration[11], and optical traps[12–15]. These techniques can access the rheological properties of a sample and their changes under various pathophysiological conditions. Yet, most of them require physical contact between probe and sample surface and none of them allows to obtain spatially resolved distributions of the mechanical properties inside the specimens.

Brillouin microscopy has emerged as a novel microscopy technique to provide label-free, non-contact, and spatially resolved measurements of the mechanical properties inside biological samples[16–18]. The technique is based on Brillouin light scattering which arises from the inelastic interaction between the incident photons and collective fluctuations of the molecules (acoustic phonons)[19,20]. The Brillouin shift measured is related to the longitudinal modulus, refractive index (RI), and absolute density of the sample (see Methods). So far, conventional Brillouin microscopy does not consider the contribution of heterogeneous RI and absolute density distributions to the longitudinal modulus. Most studies either assume a homogeneous RI distribution[16,21,22], argument that the RI and absolute density trivially cancel out[17,23,24] or use RI values obtained separately by other imaging setups[25]. These simplifications may result in an inaccurate calculation of the longitudinal modulus. Only recently, serial Brillouin measurements of samples illuminated under different illumination angles allowed measuring the RI value inside the focal volume as well[26]. However, this technique requires illuminating the sample from two different directions, which doubles the acquisition time and decreases the spatial resolution of the measurement when compared to a setup only acquiring the Brillouin shift.

Optical diffraction tomography (ODT) has been utilized for measuring the three-dimensional (3D) RI distribution of various specimens[27,28]. Employing quantitative phase imaging, ODT can reconstruct the 3D RI distribution of living biological samples from the complex optical fields measured under different illumination angles. Given the RI, the mass density of most biological samples can be calculated using a two-substance mixture model (see Methods)[29–31]. However, this requires knowledge of the refraction increment, which depends on the material composition and takes on values of $0.173\,\mathrm{ml/g}$ to $0.215\,\mathrm{ml/g}$ with an average of $0.190\,\mathrm{ml/g}$ for different human proteins[32,33] and can go down to $0.135\,\mathrm{ml/g}$ to $0.138\,\mathrm{ml/g}$ for phospholipids[34,35]. Furthermore, the two-substance mixture model does not apply to cell compartments mainly filled with a single substance, e.g. lipid droplets in adipocytes. Hence, molecular specificity by e.g. fluorescence imaging is necessary to determine whether the two-substance mixture model is appropriate and which refraction increment should be used to calculate the absolute density of a certain cell region.

Here, we present a combined optical system for epi-fluorescence, ODT, and Brillouin microscopy (FOB microscopy) which can provide the correct longitudinal modulus from colocalized measurements of the Brillouin shift and RI distributions and the subsequently calculated absolute densities of a sample. The principal function of the FOB microscope is demonstrated by measurements of cell phantoms made of biconstituent polymers with known mechanical properties. We further applied the setup to HeLa cells and adipocytes. First, we investigated two condensates that form by physical process of phase separation – nucleoli in the nucleus and stress granules in the cytoplasm[36]. Nucleoli in HeLa cells showed a higher RI and longitudinal modulus than the cytoplasm, whereas the nucleoplasm had a lower RI than the cytoplasm while still showing a higher longitudinal modulus. The RI of the cytoplasm and nucleoplasm decreased after stressing HeLa cells with arsenite, but we found no significant difference of either the RI or longitudinal modulus of stress granules to the surrounding cytoplasm. By contrast, poly-Q aggregates formed by overexpressing the aggregation-prone exon 1 of Q103 huntingtin exhibited considerable differences to the surrounding compartment in terms of RI and longitudinal modulus. Moreover, unlike water-based cellular condensates and aggregates, lipid droplets inside adipocytes showed higher RI and Brillouin shift, but lower longitudinal modulus than the cytoplasm when taking into account their absolute density. These data illustrates that in order to correctly calculate the longitudinal modulus, the RI as well as the absolute density have to be taken into account. In summary, the presented setup could provide measurement data necessary for a deeper understanding of pathophysiological processes related to cell mechanics and condensates that form by the process of phase separation.

Results

Optical setup

FOB microscopy combines ODT with Brillouin microscopy and epi-fluorescence imaging (Fig. 1a). The three imaging modalities are sequentially applied to quantitatively map the RI, the Brillouin shift, and the epi-fluorescence intensity distribution inside a given sample. These parameters allow to e.g. infer the mass density and dry mass of the sample, and provide molecular specificity for fluorescently labeled structures. Given the molecular specificity, it is furthermore possible to localize subcellular

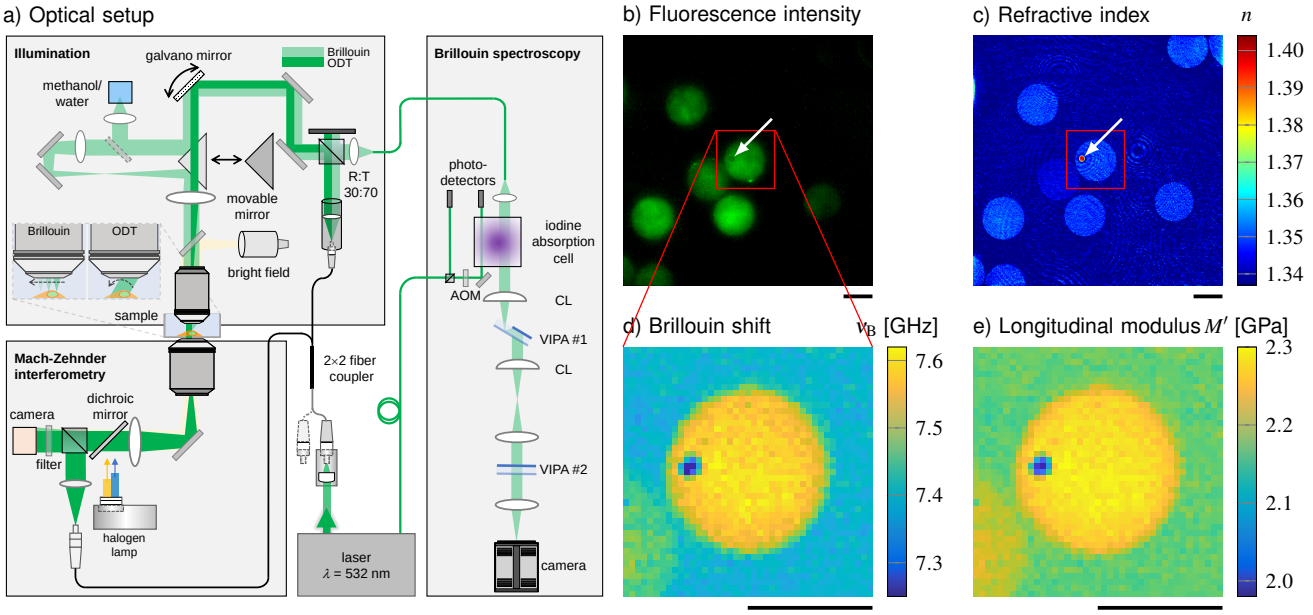

Figure 1. Combined fluorescence, optical diffraction tomography (ODT) and Brillouin microscopy. (**a**) Optical setup. The beam paths for epi-fluorescence / brightfield imaging, ODT and Brillouin microscopy are shown in light yellow, dark green and light green, respectively. The laser light illuminating the sample is collimated in ODT mode and focused in Brillouin mode. A moveable mirror enables to switch between the two modes. The Brillouin scattered light is guided to the spectrometer by a single-mode fiber, which acts as confocal pinhole. The light transmitted through the sample interferes with a reference beam. AOM, acousto-optic modulator; CL, cylindrical lens; LED, light-emitting diode; VIPA, virtually imaged phased array. (**b-e**) Quantitative and spatially resolved maps of a cell phantom consisting of a PDMS bead (indicated by the white arrows) inside a PAA bead stained with Alexa 488 (green fluorescence in (**b**)) acquired with the FOB microscope. (**b**) epi-fluorescence intensities, (**c**) refractive indices, (**d**) Brillouin shifts and (**e**) calculated longitudinal moduli. Scale bars 10 µm.

organelles of interest and to determine whether for a certain region the two-substance mixture model can be applied to calculate the local absolute density, or if the literature value of the absolute density has to be used (e.g. in lipid droplets). Finally, with the combination of RI, absolute density, and Brillouin shift distributions, the longitudinal modulus can be calculated.

For ODT, the sample is illuminated with a plane wave under different incident angles. To illuminate the sample under different angles, a dual-axis galvanometer mirror tilts the illumination beam. The transmitted light interferes with a reference beam and creates a spatially modulated hologram on a camera from which the phase delay and finally the RI of the sample is calculated with a resolution of 0.25 µm within the lateral plane and 0.5 µm in the axial direction (Fig. 1c). Epi-fluorescence microscopy captures the fluorescence emission intensity image (Fig. 1b) with the same camera used for the ODT acquisition.

For Brillouin microscopy, a moveable mirror guides the incident light to an additional lens which leads to a focus in the sample with a size of 0.4 µm in the lateral plane and approximately 1 µm in axial direction. The focus is translated by the galvanometer mirror to scan the whole sample. The Brillouin scattered light is collected in the backscattering configuration and guided to a two-stage virtually imaged phased array (VIPA) spectrometer[16]. The Brillouin shift (Fig. 1d) is extracted from the recorded Brillouin spectrum and the longitudinal modulus (Fig. 1e) is calculated from the Brillouin shift, RI and absolute density distributions acquired (see Methods).

Validation of the setup with cell phantoms

To validate the basic performance of the combined FOB microscopy setup, we acquired the RI and Brillouin shift of an artificial cell phantom with known material properties. The phantom consists of a polydimethylsiloxane (PDMS) bead embedded in a polyacrylamide (PAA) bead (Fig. 1b-e) which was fluorescently labeled with Alexa 488 (See Methods). The RI of the embedded PDMS bead was measured as 1.3920 ± 0.0012 (mean value $\pm$ SEM) (Fig. 1c). This was slightly lower than values reported for bulk PDMS with the RI of 1.416[37], which could be due to the swelling of the PDMS beads during the fabrication process[38]. The RI of the PAA bead (1.3485 ± 0.0001) was significantly lower than that of the PDMS bead, and was close to the previously reported value[39]. In contrast, the Brillouin shift of the PDMS bead (7.279 ± 0.019 GHz) was lower than for the PAA bead (7.574 ± 0.001 GHz) (Fig. 1d). In order to calculate the longitudinal modulus, the absolute density of the PAA bead (1.0190 ± 0.0001 g/ml) was calculated from the measured RI by applying a two-substance mixture model (See

Methods). However, this model cannot be applied for the PDMS bead, since the bead does not contain a fluid phase. Hence, the area of the PDMS bead was segmented based on the RI and fluorescence intensity (Fig. 1b), and the literature value for the absolute density of PDMS (1.03 g/ml) was used[40]. The resulting longitudinal modulus is shown in Fig. 1e. We found values of 2.022 ± 0.013 GPa for the PDMS bead and 2.274 ± 0.001 GPa for the PAA bead. The results are consistent with previous measurements of the speed of sound in PDMS[41] and the longitudinal modulus of PAA[25] when taking into account the absolute density of the dry fraction (i.e. (2)). Our finding clearly demonstrates the strength of the presented FOB setup to provide local RI and absolute density distributions for correctly calculating longitudinal modulus from the Brillouin shift measured.

Cell nucleoplasm has lower absolute density but higher longitudinal modulus than cytoplasm

The FOB microscope can also provide much needed quantitative insight into a biological phenomenon that has recently captured the imagination of physicists and biologists alike – the formation of membraneless compartments by liquid-liquid phase separation (LLPS)[42]. One such membraneless compartment is the nucleolus, a region within the nucleus where ribosomal subunits are synthesized. Here, we recorded the epi-fluorescence, Brillouin shift, and RI distributions of 139 HeLa cells in which a nucleolar marker protein NIFK was tagged with GFP and the nuclei were stained with Hoechst (See Methods). In order to evaluate the mechanical properties of the cytoplasm, nucleoplasm, and nucleoli separately, we segmented the different compartments of the cells based on the RI and the two-channel epi-fluorescence intensity maps (Fig. 2a, see Methods).

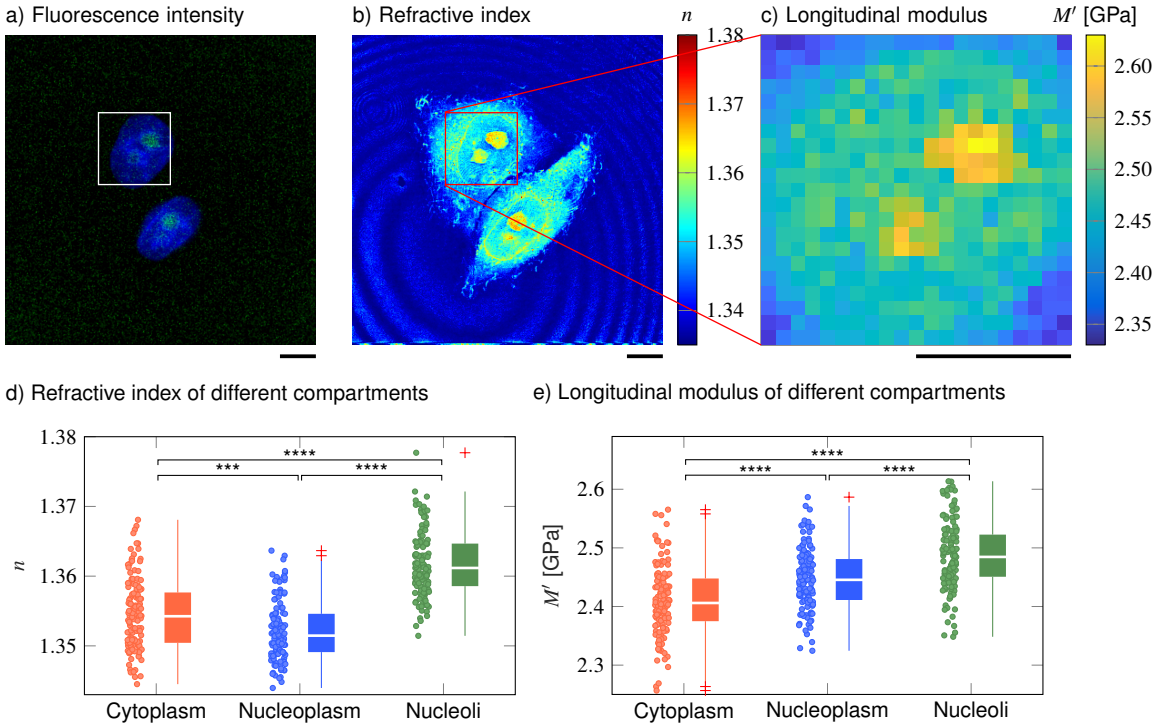

Figure 2. Cell nucleoplasm has lower RI but higher longitudinal modulus than cytoplasm. (**a-c**) Representative maps of the (**a**) epi-fluorescence intensity distribution, (**b**) longitudinal moduli and (**c**) refractive indices of a HeLa cell. Nuclei are stained with Hoechst (blue) and the nucleolar protein in the nucleoli is labeled with GFP (green). Quantitative analysis of (**d**) the refractive index and (**e**) the calculated longitudinal modulus taking into account the Brillouin shifts, refractive indices and absolute densities of 139 HeLa cells. Scale bars 10 µm. $^{***}p < 0.001$; $^{****}p < 0.0001$.

As shown in Fig. 2b and d, the nucleoplasm of HeLa cells exhibited a significantly lower RI than the cytoplasm (Kruskal-Wallis $p_{n_{\mathrm{cyto}},n_{\mathrm{np}}} = 9 \times 10^{-4}$), with values of 1.3522 ± 0.0004 (nucleoplasm) and 1.3545 ± 0.0004 (cytoplasm), which is consistent with previous studies[43,44]. Since the RI of the HeLa cells measured is linearly proportional to their mass density[44], we applied the two-substance mixture model and used a global refraction increment of 0.190 ml/g, which is valid for protein and nucleic acid[31,32], to calculate the absolute densities of each cell and its compartments. The resulting absolute densities are shown in Supplementary Fig. 1b. We found that the nucleoplasm had a lower absolute density (1.0207 ± 0.0005 g/ml) than the cytoplasm (1.0234 ± 0.0006 g/ml). Here, the perinuclear cytoplasm also contains many lipid-rich membrane-bound organelles, and the RI increment of phospholipids (0.135 ml/g to 0.138 ml/g,[34,35]) is lower than that of protein and nucleic acid. Hence,

the calculated absolute density of the cytoplasm could be underestimated and the absolute density difference between cytoplasm and nucleoplasm might be even more pronounced.

Interestingly, the Brillouin shift of the nucleoplasm (7.872 ± 0.007 GHz) was significantly higher than the value of the cytoplasm (7.811 ± 0.008 GHz) ($p_{\nu_{\mathrm{B,cyto}},\nu_{\mathrm{B,np}}} = 2 \times 10^{-6}$, Supplementary Fig. 1a). The longitudinal moduli of the nucleoplasm (2.448 ± 0.005 GPa) and cytoplasm (2.410 ± 0.005 GPa) followed the same trend as the Brillouin shifts ($p_{M'_{\mathrm{cyto}},M'_{\mathrm{np}}} = 7 \times 10^{-7}$, Fig. 2c and e). Moreover, the nucleoli, where ribosomal subunits are synthesized, exhibited significantly higher RI ($n = 1.3618 \pm 0.0004$), Brillouin shift ($\nu_{\mathrm{b}} = 7.938 \pm 0.008$ GHz), and longitudinal modulus ($M' = 2.487 \pm 0.005$ GPa) than either nucleoplasm or cytoplasm. A full list of the resulting RI, Brillouin shifts, absolute densities and longitudinal moduli and the corresponding p-values when comparing between different cell compartments can be found in the Supplementary tables 1 and 2.

These findings imply that membraneless compartments formed by phase separation, in this case the nucleolus, can maintain a higher absolute density and distinct compressibility (here, higher longitudinal modulus) in spite of the thermodynamic instability inherent in this state.

PolyQ aggregates have higher absolute density and longitudinal modulus than cytoplasm

To compare the properties of physiological condensates with a densely packed protein aggregate, we overexpressed an expanded version of the aggregation-prone exon 1 of huntingtin with 103 consecutive glutamines[45–47]. Q103 phase separates into liquid droplets in cells and these droplets rapidly convert into a solid-like state[48], meaning they do not recover from photobleaching when subjected to fluorescence recovery after photobleaching (FRAP) experiments[49]. Here, we observe polyglutamine (polyQ) aggregates labeled with GFP in transiently transfected wild-type HeLa cells. We used the FOB microscope to measure the mechanical properties of polyQ granules in 22 cells.

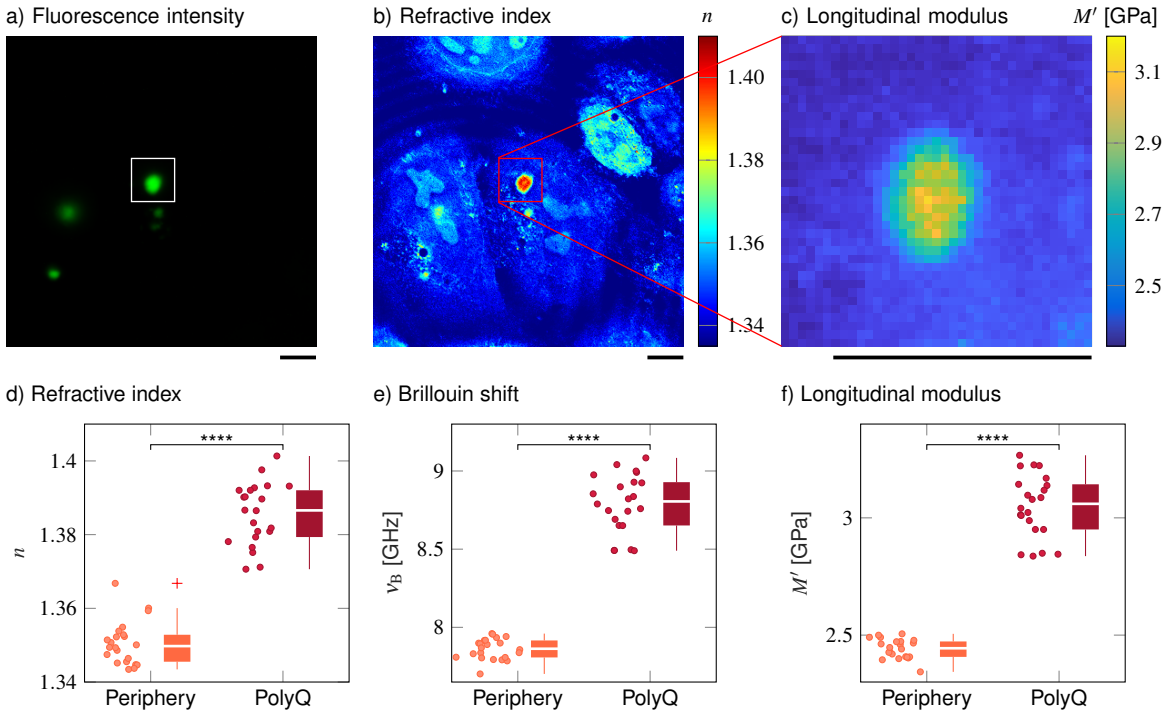

Figure 3. PolyQ aggregates have a higher refractive index, Brillouin shift and longitudinal modulus than the peripheral cytoplasm. (**a-c**) Representative maps of (**a**) the epi-fluorescence intensity distribution, (**b**) the refractive indices and (**c**) the longitudinal moduli of a HeLa cell transfected with a plasmid encoding HttQ103. The polyQ aggregates are labeled with GFP (green). Quantitative analysis of (**d**) the refractive index, (**e**) the Brillouin shift and (**f**) the calculated longitudinal modulus taking into account the Brillouin shifts, refractive indices and absolute densities of 22 polyQ granules. Scale bars 10 µm. $^{****}p < 0.0001$.

The polyQ aggregates showed a strong fluorescence signal in the GFP channel (Fig. 3a). We hence used the fluorescence intensity to segment the aggregates from the peripheral cytoplasm in order to quantitatively compare cytoplasm and aggregates (Fig. 3b and c). The RI (1.3856 ± 0.0018) and the longitudinal modulus (3.051 ± 0.029 GPa) of the aggregates

were significantly higher ($p < 0.0001$) than the RI (1.3506 ± 0.0013) and longitudinal modulus (2.442 ± 0.009 GPa) of the peripheral cytoplasm (Fig. 3d and f and Supplementary table 3). Our results show that FOB microscopy can quantify the physical properties of cytoplasmic membraneless condensates – in principle.

GFP-FUS stress granules in P525L HeLa cells show RI and longitudinal modulus similar to the surrounding cytoplasm

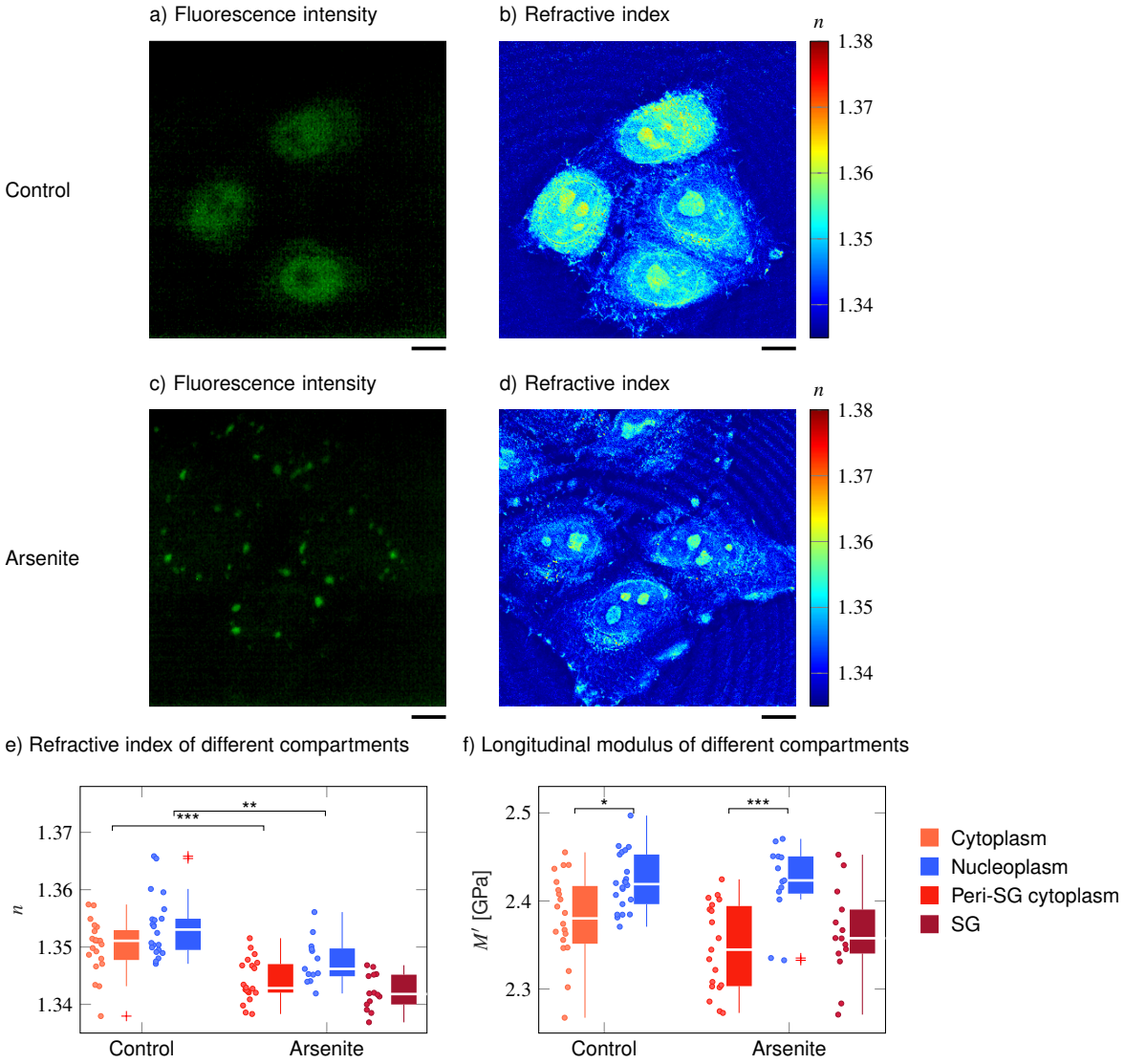

Figure 4. GFP-FUS-labelled stress granules induced by oxidative stress in P525L FUS HeLa cells show a similar RI and longitudinal modulus as the peripheral cytoplasm. Representative example of (**a**) the fluorescence intensity and (**b**) the refractive index distribution under control conditions without arsenite, and (**c**) the fluorescence intensity and (**d**) the refractive index distribution with arsenite. Quantitative analysis of (**e**) the refractive index and (**b**) the calculated longitudinal modulus taking into account the Brillouin shift and refractive index. $^{*}p < 0.05$; $^{**}p < 0.01$; $^{***}p < 0.001$.

Recently, another type of condensates formed by LLPS — RNA and protein (RNP) granules, such as stress granules (SGs) — has received much attention, due to their linkage to neurodegenerative diseases such as amyotrophic lateral sclerosis (ALS) and frontotemporal dementia[50,51]. It is also increasingly recognized that the mechanical properties of these compartments influence their functions and involvement in disease[52,53]. Fused in sarcoma (FUS) protein, an RNA-binding protein involved in DNA repair and transcription, is one example of a protein that localizes to SGs[50]. Purified FUS protein is able to phase separate into liquid condensates in vitro, and this property is important for FUS to localize to SGs. Disease-linked mutations in FUS

have been shown to promote a conversion of reconstituted liquid FUS droplets from a liquid to a solid state, suggesting that an aberrant liquid to solid transition of FUS protein promotes disease.

Conventionally, the mechanical changes of SGs have been indirectly characterized by FRAP or observing fusion events of liquid droplets[54]. Recently, Brillouin microscopy was used to measure the Brillouin shift of SGs in chemically fixed P525L HeLa cells expressing mutant RFP-tagged FUS under doxycycline exposure[24]. P525L HeLa cells are used as a disease model for ALS and form SGs under arsenite stress conditions. It was shown that the Brillouin shift of SGs induced by arsenite treatment with mutant RFP-FUS is significantly higher than the Brillouin shift of SGs without mutant RFP-FUS. Furthermore, the Brillouin shift of mutant RFP-FUS SGs was reported to be significantly higher than the value of the surrounding cytoplasm[24].

Here, we applied the FOB setup to P525L HeLa cells which express GFP-tagged FUS, and quantified the RI distributions, epi-fluorescence intensities, and Brillouin shifts of the nucleoplasm, cytoplasm, and SGs. The cells were measured under control conditions or when exposed to 5 mM sodium arsenite $NaAsO_2$ 30 min prior to the measurements. Since the SGs are not static, and assemble and disassemble dynamically, acquiring the Brillouin shift map of a complete cell would be to slow, which was the reason for fixing the cells in a previous study[24]. During the approximate duration of 20 min to 30 min of a whole cell measurement, SGs moved significantly or even disassembled and, hence, did not colocalize with their epi-fluorescence signal acquired before. Furthermore, the P525L GFP-FUS HeLa cells reacted sensitively to the exposure to green laser light and suffered from cell death during a whole cell measurement. We therefore acquired the Brillouin shift of a small region of 5 µm by 5 µm only, which reduced the duration to less than 2 min, allowing us to colocalize the SGs Brillouin shift and epi-fluorescence signal, preventing cell death during acquisition. The positions for the Brillouin shift measurements of the different compartments were chosen manually based on the epi-fluorescence and brightfield intensities (see Fig. 4a-d).

We found that, in difference to wild-type HeLa cells, the RI of the cytoplasm ($n_{\mathrm{cyto}} = 1.3500 \pm 0.0010$) and the RI of the nucleoplasm ($n_{\mathrm{nucleo}} = 1.3535 \pm 0.0011$) were not significantly different ($p > 0.05$) (Fig. 4e) and the RI of the nucleoplasm was even slightly higher than the RI of the cytoplasm. However, when segmenting the RI of the whole cell and not only taking into account the RI of the manually selected regions for which we also performed measurements of the Brillouin shift, we found a slightly lower RI in the nucleoplasm ($n_{\mathrm{nucleo,global}} = 1.3515 \pm 0.0004$) than in the cytoplasm ($n_{\mathrm{cyto,global}} = 1.3521 \pm 0.0004$) (Supplementary Fig. 2). Hence, we think the slightly higher RI of the nucleoplasm was an artefact of the manual selection of the measurement positions. As for wild-type HeLa cells, the longitudinal modulus of the nucleoplasm ($M'_{\mathrm{nucleo}} = 2.421 \pm 0.007\,\mathrm{GPa}$) was significantly higher than the modulus of the cytoplasm ($M'_{\mathrm{cyto}} = 2.380 \pm 0.011\,\mathrm{GPa}$, $p = 0.01$, Fig. 4f). While the GFP-tagged FUS of the control cells was mainly located in the nucleoplasm (Fig. 4a), after arsenite treatment the FUS was relocated from the nucleoplasm and aggregated in SGs within the cytoplasm (Fig. 4c). This was accompanied by a significant decrease of the RI of both the peri-SG cytoplasm ($n_{\mathrm{peri-cyto}} = 1.3442 \pm 0.0008, p = 0.0003$) and the nucleoplasm ($n_{\mathrm{nucleo}} = 1.3475 \pm 0.0011, p = 0.0054$). Even after the arsenite treatment, there were no significant differences between the RI of the peri-SG cytoplasm and the nucleoplasm ($p > 0.05$, Supplementary Fig. 2). Furthermore, we found no significant difference of neither the RI ($n_{\mathrm{SG}} = 1.3422 \pm 0.0008$) nor the longitudinal modulus ($M'_{\mathrm{SG}} = 2.362 \pm 0.014\,\mathrm{GPa}$) of SGs to the respective values of the peri-SG cytoplasm. Although the longitudinal modulus did not change significantly due to the arsenite treatment, the difference between the longitudinal modulus of the peri-SG cytoplasm ($M'_{\mathrm{cyto}} = 2.347 \pm 0.012\,\mathrm{GPa}$) and the nucleoplasm ($M'_{\mathrm{cyto}} = 2.421 \pm 0.012\,\mathrm{GPa}$) was more pronounced after the arsenite treatment ($p = 0.0001$, Fig. 4f).

Altogether, in P525L HeLa cells expressing GFP-FUS the RI of the cytoplasm and nucleoplasm showed no significant differences in untreated cells and decreased significantly after arsenite treatment. For both the control and arsenite treated cells, the longitudinal modulus of the nucleoplasm was significantly higher than the modulus of the cytoplasm in terms of RI and longitudinal modulus. Interestingly, SGs showed no significant differences to the peri-SG cytoplasm. This is inconsistent to a previous study showing a higher longitudinal modulus of SGs compared to cytoplasm[24]. However, in the previous study, a different cell line expressing RFP-tagged FUS was used and the cells measured were chemically fixed. These differences might explain the discrepancy of the results, especially since fixation can significantly alter the mechanical[55] as well as the optical properties[56] of biological samples.

Mechanical characterization of lipid droplets in adipocytes requires precise RI and density

Most biological cells can be thought of as a mixture of ions and macromolecules such as proteins, nucleic acids, and sugars dissolved in water, for which the two-substance mixture model[29–31] is appropriate to describe the relationship between the RI and the absolute density. However, this is not the case for special compartments in certain cell types. The lipid droplets within adipocytes are not composed of a water-based solution and cannot be characterized by the two-substance mixture model. To overcome this problem, we exploit the molecular specificity of the FOB setup to identify and segment the lipid droplets. Since previous mass spectroscopy studies on adipocyte cell culture models have identified palmitoyl triacylglycerides as predominant lipid species[57,58], we use an absolute density value of $0.8932\,\mathrm{g/ml}$ for calculating the longitudinal moduli of the lipid droplets.

Here, we observed Simpson-Golabi-Behmel Syndrome (SGBS) adipocytes[59] whose nucleus and lipid droplets were stained with Hoechst and Nile red respectively on day 11 of adipogenic differentiation. The lipid droplets were clearly visible in

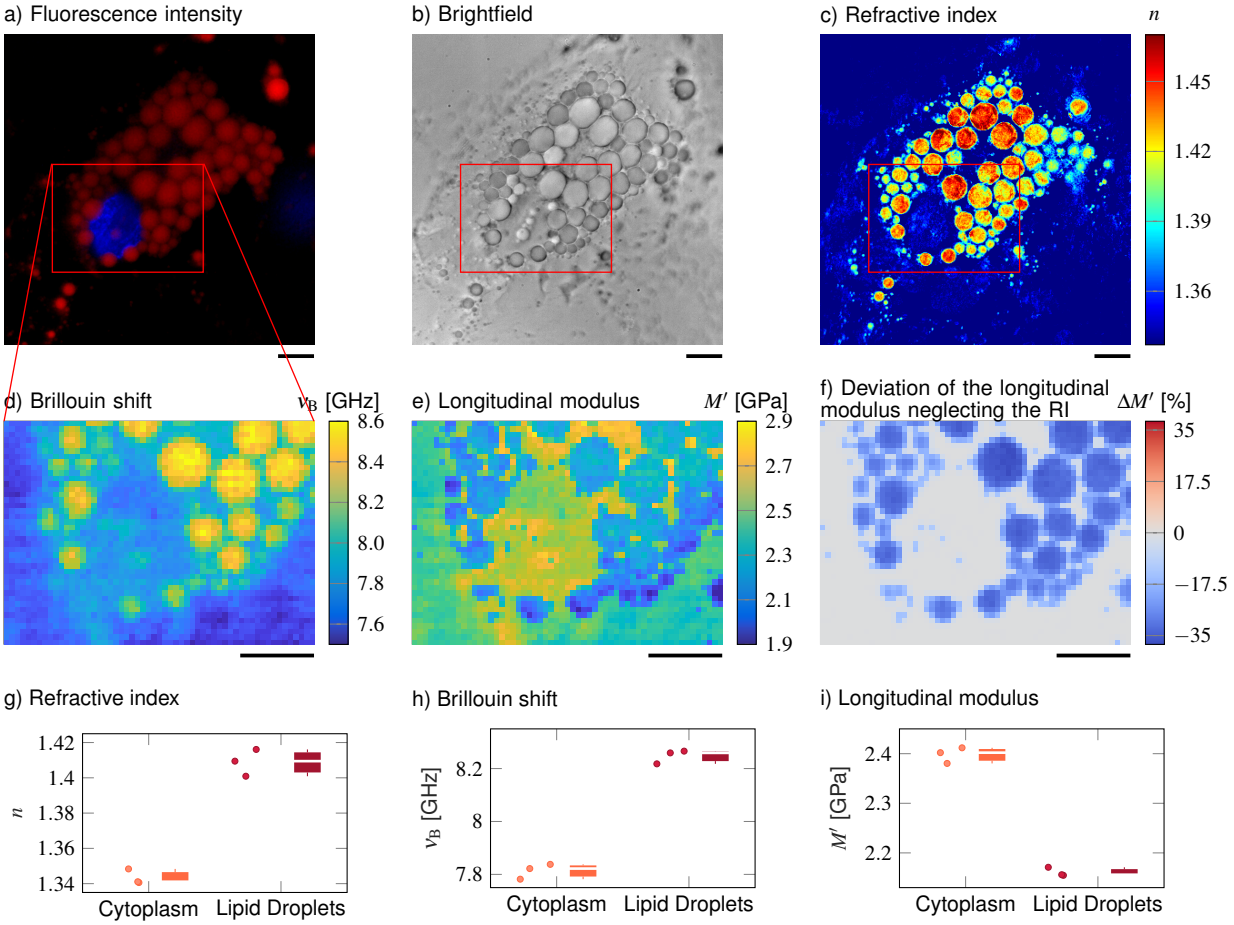

Figure 5. Despite a higher RI and Brillouin shift, the longitudinal modulus of lipid droplets is lower than of the surrounding cytoplasm. (**a-d**) Representative maps of the (**a**) epi-fluorescence intensities, (**b**) brightfield intensities, (**c**) refractive indices and (**d**) Brillouin shifts of an adipocyte cell. The nucleus is stained with Hoechst (blue in (**a**)) and lipid droplets are stained with Nile red (red in (**a**)). (**e**) Longitudinal modulus calculated from the refractive indices, absolute densities and Brillouin shifts. (**f**) Deviation of the longitudinal modulus calculated with a homogeneous refractive index and absolute density value when compared to the precise longitudinal modulus in (**e**). Quantitative analysis of (**g**) the refractive index, (**h**) the Brillouin shift and (**i**) the calculated longitudinal modulus taking into account the Brillouin shifts, refractive indices and absolute densities of 3 adipocytes. Scale bar 10 µm

the fluorescence intensity (Fig. 5a) and showed a high mean RI value of 1.409 ± 0.004 (Fig. 5c). The Brillouin shift of the lipid droplets of 8.25 ± 0.02 GHz was also significantly higher than the Brillouin shift of the surrounding cytoplasm of 7.81 ± 0.02 GHz (Fig. 5d). Hence, one could expect that the longitudinal modulus shows a similar trend as the Brillouin shift as it does for samples described by the two-substance mixture model. However, the longitudinal modulus of the lipid droplets (2.161 ± 0.005 GPa) was lower than that of the cytoplasm (2.398 ± 0.009 GPa) when the measured RI and extracted absolute density distributions were considered (Fig. 5e). The longitudinal modulus of lipid droplets being lower than that of cytoplasm was consistent with previous measurement data of the speed of sound of triacylglycerides which is lower than that of water[60]. In order to demonstrate the effect of the RI and absolute density on the calculation of the longitudinal modulus, we calculated the longitudinal modulus under the assumption of a homogeneous RI (1.337) and absolute density (1 g/ml) distribution instead of the values measured, as it would likely be done for a stand-alone Brillouin microscope. The longitudinal modulus of lipid droplets without considering the RI and absolute densities measured results to 2.717 ± 0.022 GPa, which was 26 % higher than the correctly calculated longitudinal modulus (Fig. 5f). Our finding clearly demonstrates that the local distribution of RI and absolute density can contribute considerably to the extraction of the longitudinal modulus of the samples, especially for compartments which cannot be described by the water-based two-substance mixture model.

Discussion

In this report, we experimentally demonstrated a combined epi-fluorescence, ODT, and Brillouin (FOB) microscopy setup. The colocalized measurements and the subsequent image analysis of the epi-fluorescence intensities and the RI distributions acquired by the FOB setup allowed to identify regions of different material or molecular composition. This enabled us to extract the correct absolute density from either the RI measured by applying the two-substance mixture model, or from the literature in case the two-substance mixture model is not applicable. In combination with the Brillouin shift distributions measured, it was possible to accurately calculate the longitudinal moduli of a specimen. Especially for samples with heterogeneous RI and absolute density distributions, this is a major improvement over setups only capable of acquiring the RI or Brillouin shift separately, as demonstrated for an artificial cell phantom consisting of a PDMS bead embedded in a PAA bead. The acquired longitudinal moduli values are consistent with previous studies only when we consider the RI and the absolute density of the PDMS and PAA bead.

The setup was also applied to investigate the physical and mechanical properties of intracellular compartments in HeLa cells including nucleoplasm, cytoplasm, and nucleoli. We found that the nucleoplasm has a lower RI and absolute density than the cytoplasm while showing a higher Brillouin shift and longitudinal modulus. Moreover, nucleoli, which are formed by liquid-liquid phase separation (LLPS) in the nucleoplasm, and polyQ aggregates, which undergo a rapid liquid-to-solid transition in the cytoplasm, exhibit a significantly higher RI and longitudinal modulus than either nucleoplasm or cytoplasm. However, SGs in P525L HeLa cells, which are also formed by LLPS, did not show significant differences in terms of RI or longitudinal modulus compared to the surrounding cytoplasm. Hence, it seems that not every condensation process is accompanied by changes of the RI, absolute density or longitudinal modulus. Further investigation is required to reveal the underlying mechanism of how nucleoli consisting of proteins and nucleic acids maintain a higher density and longitudinal modulus than the surrounding nucleoplasm despite the dynamic behavior of compartments formed by LLPS[61].

Currently, there is a vivid debate whether the Brillouin shift mainly depends on the water content of the specimen, not on its mechanical properties[62–65]. If we followed the idea that the water content dominates the Brillouin shift, samples with a higher water content would exhibit a lower Brillouin shift. As the RI of the cytoplasm and the nucleoplasm of the HeLa cells measured here is linearly proportional to the mass density of macromolecules in water solution[29,30] and the refraction increments of both compartments are similar[31,32], the lower RI of the nucleoplasm compared to the cytoplasm indicates that the nucleoplasm has a higher water content than the cytoplasm. However, the nucleoplasm exhibits a higher Brillouin shift and longitudinal modulus than the surrounding cytoplasm. Hence, this result indicates that the Brillouin shift and the longitudinal modulus are not only governed by the water content, but are at least significantly influenced by the mechanical properties of the specimen.

An important aspect of the calculation of the longitudinal moduli is the extraction of the precise densities of the samples. For samples or compartments that can be described by the two-substance mixture model, we exploited the linear relation between the RI and the mass density to calculate the absolute density value[29–31]. For cell compartments mainly containing a single substance, where this model cannot be applied, e.g. lipid droplets in adipocytes, we used the molecular specificity provided by the epi-fluorescence imaging to identify the respective regions and employed the literature value for the absolute density in this region. Using this approach, we found that although the RI and Brillouin shift of the lipid compartments in adipocytes are higher than those values of the cytoplasm, the resulting longitudinal modulus is actually lower when taking into account the RI and absolute density distribution. This illustrates that RI and absolute density do not cancel out for every cell and compartment – an implict assumption in many studies acquiring only the Brillouin shift – and that RI and absolute density have to be known in order to precisely calculate the longitudinal modulus.

However, both the calculation of the absolute density from the RI and the identification of regions not described by the two-substance mixture model rely on the knowledge of the molecular composition of the sample. In order to calculate the absolute density from the RI, the refraction increment has to be known, which, albeit comparable for proteins and nucleic acids, might slightly vary between different cell compartments depending on their composition. Obviously, the composition also plays an important role when selecting the correct literature value for the absolute density of compartments where the two-substance mixture model is not applicable. As the molecular composition cannot be resolved exactly by the FOB microscope, we used the refraction increment or absolute density of the constituent likely predominant in a certain compartment. This might lead to a slight deviation of the absolute density from the exact value, e.g. in the membrane-rich perinuclear region of HeLa cells where the absolute density might be underestimated. To overcome this issue and use the appropriate refraction increment or absolute density for a mixture of different proteins, nucleic acids, or phospholipids, more sophisticated labeling and staining of different molecules and the use of several fluorescence channels might allow identifying multiple substances. Also, the absolute concentration of different molecules could be directly measured from the intensity of Raman scattering signals[66], an imaging extension that could be added for future studies to the FOB setup presented here[67].

In conclusion, the FOB setup allows a precise calculation of the longitudinal modulus from the measured RI and Brillouin shift even for samples with a heterogeneous RI and absolute density distribution. This enables quantitative measurements of the mechanical properties of single cells and their compartments and could lead to a deeper understanding of physiological and

pathological processes such as phase separation and transition in cells as a response to external stress.

Methods

Optical setup

The FOB microscope setup combines optical diffraction tomography (ODT), Brillouin microscopy and epi-fluorescence imaging in the same optical system. It allows to obtain quantitative maps of the refractive indices (RI), the Brillouin shifts, and the fluorescence and brightfield intensities of a sample.

In order to acquire the three-dimensional RI distribution, ODT employing Mach-Zehnder interferometry is applied. Besides small modifications necessary for the combination with Brillouin microscopy the ODT part of the setup is identical to the one presented in[68]. As laser source a frequency-doubled Nd-YAG laser (Torus 532, Laser Quantum Ltd, United Kingdom) with a wavelength of 532 nm and a maximum output power of 750 mW is used for both ODT and Brillouin microscopy. The main beam of the laser is coupled into a single-mode fiber and split into two beams by a 2×2 fiber coupler. One beam is used as the reference for the Mach-Zehnder interferometer. The other beam is collimated and demagnified through a tube lens with a focal length of 175 mm and a 40x/1.0 NA water dipping objective lens (Carl Zeiss AG, Germany), and illuminates the sample in a custom-built inverted microscope. To allow to reconstruct a three-dimensional RI tomogram of the sample, the sample is illuminated under 150 different incident angles. The illumination angles are generated by a dual-axis galvanometer mirror (GVS012/M, Thorlabs Inc., USA) which is placed at the conjugate plane of the sample and diffracts the illumination beam. The diffracted beam is collected by a 63x/1.2 NA water immersion objective lens (Carl Zeiss AG, Germany) and a tube lens with a focal length of 200 mm. The sample and the reference beam then interfere at the image plane of a CCD camera (FL3-U3-13Y3M-C, FLIR Systems Inc., USA) which records the generated spatially modulated hologram. The setup achieves a spatial resolution of 0.25 µm within the lateral plane and 0.5 µm in the axial direction.

In order to switch to Brillouin microscopy mode, a motorized mirror is moved into the beam path guiding the light towards an additional lens with a focal length of 300 mm. In combination with the upper tube lens this ensures a collimated beam before the microscope objective and effectively creates a laser focus at the sample plane. Hence, in Brillouin mode the galvanometer mirrors are located at the Fourier conjugate plane of the sample and can move the laser focus in the sample plane (Fig. 1a, inset). This allows to scan the laser focus over the sample by adjusting the galvanometer voltage. The relation between the applied galvanometer voltage and the resulting focus position is calibrated by acquiring images of the laser foci with the ODT camera and extracting the foci positions for different galvanometer voltages. The Brillouin scattered light is collected in the backscattering configuration with the same objective used for ODT and coupled into a single-mode fiber which acts as a pinhole confocal to the illumination fiber and delivers the light to a two-stage virtually imaged phased array (VIPA) Brillouin spectrometer[17,69]. This results in a spatial resolution of 0.4 µm within the lateral plane and approximately 1 µm in the axial direction. In the spectrometer the beam is collimated and passes through the iodine absorption cell, which blocks the Rayleigh scattered and reflected light. The beam is then guided to two VIPA interferometers (OP-6721-3371-2, Light Machinery, Canada) with 30 GHz free spectral range. The Brillouin spectrum is imaged with an sCMOS camera (Neo 5.5, Andor, USA).

Furthermore, the laser frequency is stabilized to the absorption maximum of a transition line of molecular iodine by controlling the laser cavity temperature. This allows to attenuate the intensity of the Rayleigh scattered light entering the Brillouin spectrometer and eliminates potential laser frequency drifts[25,70]. To generate an error signal for the frequency stabilization loop a small fraction of the laser light is frequency shifted by 350 MHz by an acousto-optic modulator (AOM 3350-125, EQ Photonics GmbH, Germany) and guided through an absorption cell (TG-ABI-Q, Precision Glass Blowing, USA) filled with iodine I_2. The beam intensity is measured before and after the absorption cell by two photodetectors (PDA36A2, Thorlabs Inc., USA) and a data acquisition card (PicoScope 2205A, Pico Technology, United Kingdom). The quotient of both intensities is a measure for the absorption due to the iodine vapor. The laser cavity temperature is then controlled with a custom C++ software (https://github.com/BrillouinMicroscopy/LQTControl) to achieve an absorption of 50 % for the frequency shifted stabilization beam, which leads to maximum absorption for the not shifted main beam.

To realise epi-fluorescence imaging, an incoherent beam from a white light halogen lamp (DC-950, Dolan-Jenner Industries Inc., USA) is coupled into the setup by a three-channel dichroic mirror (FF409/493/596-Di01-25x36, Semrock, USA). The bandwidth of the excitation and emission beam is selected by two motorized filter sliders equipped with band-pass filters in front of the halogen lamp and the CCD camera. A white light LED (Thorlabs, USA) coupled into the Brillouin illumination path allows to observe a brightfield image of the sample during Brillouin acquisition.

The two cameras and all moveable optical devices of the setup are controlled with a custom acquisition program written in C++. The software allows to control all three imaging modalities and stores the acquired data as an HDF5 file. The source code can be found at https://github.com/BrillouinMicroscopy/BrillouinAcquisition.

Refractive index tomogram reconstruction

From the spatially modulated holograms recorded, the complex optical field of the light scattered by the sample is retrieved by a field retrieval algorithm based on the Fourier transform[71]. The RI tomogram of the sample is reconstructed from the retrieved optical fields with various incident angles via the Fourier diffraction theorem. The detailed procedure for the tomogram reconstruction is presented in[72,73]. The field retrieval and tomogram reconstruction were performed by custom-made MATLAB (The MathWorks, Natick, USA) scripts. From the reconstructed RI tomograms, subcellular compartments are segmented based on the RI and epi-fluorescence signals. First, cell regions are segmented from background by applying the Otsu's thresholding method, and the watershed algorithm is used to determine individual cells in the RI tomograms. Then, epi-fluorescence images of the fluorescence-labeled subcellular compartments (e.g., nuclei, polyQ aggregates in HeLa cells, nuclei and lipid droplets in adipocytes) are colocalized with the RI tomograms to segment the compartments. In the nuclei of the HeLa cells, the RI tomogram regions having higher RI values than surrounding nucleoplasm are segmented by the Otsu's thresholding method and identified as nucleoli. The detailed segmentation procedure is described elsewhere[43,44], and the source code for the segmentation can be found at https://github.com/OpticalDiffractionTomography/NucleiAnalysis.

Brillouin shift evaluation

To evaluate the Brillouin shift ν_B, a custom MATLAB program is used. The software can be downloaded from https://github.com/BrillouinMicroscopy/BrillouinEvaluation. Details of the evaluation process can be found in[25].

Calculation of the longitudinal modulus

The longitudinal modulus M' is determined by

$$M' = \rho \left(\frac{\lambda \nu_B}{2n \cos(\Theta/2)} \right)^2 \tag{1}$$

where the wavelength λ of the laser source and the scattering angle Θ are known parameters of the setup. The RI n and the Brillouin shift ν_B of the sample are measured using the FOB microscope. The absolute density ρ can be calculated for the majority of biological samples from the RI assuming a two-substance mixture. The absolute density is given by[25,29–31,74]

$$\rho = \frac{n - n_{\text{fluid}}}{\alpha} + \rho_{\text{fluid}} \cdot \left(1 - \rho_{\text{dry}} \cdot \bar{\nu}_{\text{dry}}\right). \tag{2}$$

with the RI n_{fluid} of the medium, the refraction increment α ($\alpha = 0.190\,\text{mL/g}$ for proteins and nucleic acid[31,32]), the absolute density ρ_{fluid} of the medium, the absolute density ρ_{dry} and the partial specific volume $\bar{\nu}_{\text{dry}}$ of the dry fraction. In case of $\rho_{\text{dry}} \ll \frac{1}{\bar{\nu}_{\text{dry}}}$ this can be simplified to

$$\rho \approx \frac{n - n_{\text{fluid}}}{\alpha} + \rho_{\text{fluid}}. \tag{3}$$

This simplification leads to an overestimation of the absolute density of around 10 % for e.g. HeLa cells, which we believe to be acceptable.

For certain cell types, e.g. adipocyte cells, the two-substance mixture model cannot be applied for all cell compartments, i.e. the lipid droplets inside these cells do only consist of lipids. Applying the two-substance model here leads to an unphysiological overestimation of the absolute density. Hence, in special cases the absolute density cannot be inferred from the RI and has to be estimated from the literature. This is possible with the FOB microscope, since fluorescence labeling of the lipid droplets gives molecular specificity and allows to identify cell regions governed by e.g. lipids.

In order to calculate the longitudinal modulus and visualize the measurement results of the FOB microscope, a custom MATLAB program is used (https://github.com/BrillouinMicroscopy/FOBVisualizer).

Statistical analysis

For the statistical analysis of the RI and longitudinal modulus differences between cytoplasm, nucleoplasm and nucleoli (Fig. 2 and Supplementary Fig. 1) the Kruskal-Wallis test in combination with a least significant difference post-hoc test was used. The shown asterisks indicate the significance levels: $^{*}p < 0.05$, $^{**}p < 0.01$, $^{***}p < 0.001$ and $^{****}p < 0.0001$.

Cell phantom preparation

Artificial cell phantoms, consisting of polydimethylsiloxane (PDMS, Dow Corning Sylgard® 184) particles embedded in larger polyacrylamide microgel beads, were produced as follow. The PDMS particles were generated by vortex-mixing a solution of 1 g PDMS (10:1 w/w, base/curing agent) dispersed in 10 ml of 2 % w/v poly(ethylene glycol) monooleate (Merck Chemicals GmbH, Germany) aqueous solution. After mixing, the emulsion was kept overnight in an oven at 75 °C to allow the

polymerization of the PDMS droplets. The size dispersion of the PDMS particle was reduced by centrifugation and removing all particles with a diameter larger than 5 µm. The final solution, containing PDMS particles with a diameter lower than 5 µm, was washed three times in Tris-buffer (pH 7.48) and resuspended in 1 % w/v Pluronic® F-127 (Merck Chemicals GmbH, Germany) Tris-Buffer.

1 µl of concentrated PDMS particles were added to 100 µl polyacrylamide pre-gel mixture with a total monomer concentration of 11.8 % w/v. This solution was used as a dispersed phase in a flow-focusing microfluidic device to produce PAAm microgel beads, as previously described in[39], embedding PDMS particles. N-hydroxysuccinimide ester (0.1 % w/v, Merck Chemicals GmbH, Germany) was added to the oil solution to functionalize the phantoms with Alexa 488. Precisely, 100 µl of Alexa Fluor™ hydrazide 488 (ThermoFisher Scientific, Germany) in deionized water (1 mg/ml) was added to 100 µl phantom pellet and incubated overnight at 4 °C. The unbonded fluorophores were removed by three washings in PBS. The final functionalized phantoms were stored in PBS at 4 °C.

Cell preparation

The stable HeLa cell line expressing GFP fused to the N terminus of NIFK (Nucleolar protein interacting with the FHA domain of MKI67), was kindly provided by the lab of Anthony Hyman (Max Planck Institute of Molecular Cell Biology and Genetics). The cells were cultured in Dulbecco's modified Eagle's medium (DMEM) (31966-021, Thermo Fisher), high glucose with GlutaMax medium (61965-026, Gibco) under standard conditions at 37 °C and 5 % CO_2. The culture medium was supplemented with 10 % fetal bovine serum (FBS) and 1 % penicillin-streptomycin. The cells were subcultured in a glass-bottom Petri dish (FluoroDish, World Precision Instruments Germany GmbH) one day prior to the measurement, and the culture medium was exchanged to Leibovitz's L-15 Medium without phenol red (21083027, Thermo Fisher Scientific) prior to imaging. For staining nuclei, the cells were stained with Hoechst (1:1000 dilution) for 10 min and washed with fresh Leibovitz's L-15 medium prior to imaging.

The wild-type HeLa cells transiently expressing amyloid (Q103-GFP) aggregates were cultured in DMEM (31966-021, Thermo Fisher), high glucose with GlutaMax medium (61965-026, Gibco) under standard conditions at 37 °C and 5 % CO_2. The culture medium was supplemented with 10 % fetal bovine serum (FBS) and 1 % penicillin-streptomycin. The cells were subcultured in a glass-bottom Petri dish (FluoroDish, World Precision Instruments Germany GmbH) two days prior to the measurement. One day prior to the measurement the cells were transiently transfected with pcDNA3.1-Q103-GFP using Lipofectamine 2000 (Invitrogen, Carlsbad, California). Directly before the imaging the culture medium was exchanged to Leibovitz's L-15 Medium without phenol red (21083027, Thermo Fisher Scientific).

The HeLa cells GFP-FUS WT (wild-type) and GFP-FUS^{P525L} (disease model for amyotrophic lateral sclerosis) were cultured in 89 % DMEM supplemented with 10 % FBS (Sigma-Aldrich; F7524) and 1 % penicillin-streptomycin under standard conditions at 37 °C and 5 % CO_2. One day before the experiment the cells were transferred to a 35 mm glass-bottom Petri dish (FluoroDish, World Precision Instruments Germany GmbH). 30 min prior to the measurements the culture medium was exchanged to Leibovitz's L-15 medium without phenol red (21083027, Thermo Fisher Scientific) and the non-control samples were treated with 5 mM sodium arsenite.

Adipocyte preparation

Simpson-Golabi-Behmel Syndrome (SGBS) preadipocytes were cultured and differentiated as described previously[59,75]. For regular cell culture, cells were maintained in Dulbecco's modified Eagles' Medium (DMEM)/nutrient F-12 Ham (Thermofisher) supplemented with 4 µM panthotenic, 8 µM biotin (Pan/Bio), 100 U/ml penicillin/100 µg/ml streptomycin (=OF-medium) with 10 % FBS (OF-medium +FBS, Thermofisher) at 37 °C in T75 flasks. For adipogenic differentiation, cells were washed with PBS, detached using TrypLE Express (Thermofisher) and seeded onto glass-bottom Petri dishes (FluoroDish, World Precision Instruments Germany GmbH, 35 mm, 10^5 cells). After 24 hours, cells were washed three times with serum-free OF-Medium, and differentiation medium was added, consisting of OF-medium complemented with 10 µg/ml human transferrin (Sigma-Aldrich), 20 nM human insulin (Sigma-Aldrich), 2 µM rosiglitazone (Cayman), 100 nM desxamethasone (Sigma-Aldrich), 250 µM 3-isobutyl-1-1methylxantine IBMX (Sigma-Aldrich), 100 nM cortisol (Sigma-Aldrich) and 0.2 nM triiodothyronine T3 (Sigma-Aldrich). On day 4, the medium was exchanged to OF-medium supplemented with only transferrin, insulin, cortisol, T3 (concentrations as above). The medium was replaced every fourth day. Cells were probed on day 11 of adipogenic differentiation.

References

1. Engler, A. J., Sen, S., Sweeney, H. L. & Discher, D. E. Matrix Elasticity Directs Stem Cell Lineage Specification. *Cell* **126**, 677–689 (2006).
2. Provenzano, P. P. *et al.* Collagen reorganization at the tumor-stromal interface facilitates local invasion. *BMC medicine* **4**, 38 (2006).
3. Lo, C. M., Wang, H. B., Dembo, M. & Wang, Y. L. Cell movement is guided by the rigidity of the substrate. *Biophys. J.* **79**, 144–152 (2000).
4. Mammoto, T., Mammoto, A. & Ingber, D. E. Mechanobiology and Developmental Control. *Annu. Rev. Cell Dev. Biol.* **29**, 27–61 (2013).
5. Jansen, K. A. *et al.* A guide to mechanobiology: Where biology and physics meet. *Biochimica et Biophys. Acta (BBA) - Mol. Cell Res.* **1853**, 3043–3052 (2015).
6. Mohammed, D. *et al.* Innovative Tools for Mechanobiology: Unraveling Outside-In and Inside-Out Mechanotransduction. *Front. Bioeng. Biotechnol.* **7** (2019).
7. Christ, A. F. *et al.* Mechanical difference between white and gray matter in the rat cerebellum measured by scanning force microscopy. *J. Biomech.* **43**, 2986–2992 (2010).
8. Koser, D. E., Moeendarbary, E., Hanne, J., Kuerten, S. & Franze, K. CNS Cell Distribution and Axon Orientation Determine Local Spinal Cord Mechanical Properties. *Biophys. J.* **108**, 2137–2147 (2015).
9. Gautier, H. O. *et al.* Atomic force microscopy-based force measurements on animal cells and tissues. In *Methods in Cell Biology*, vol. 125, 211–235 (Elsevier, 2015).
10. Franze, K., Janmey, P. A. & Guck, J. Mechanics in Neuronal Development and Repair. *Annu. Rev. Biomed. Eng.* **15**, 227–251 (2013).
11. Maître, J.-L. *et al.* Adhesion Functions in Cell Sorting by Mechanically Coupling the Cortices of Adhering Cells. *Sci.* **338**, 253–256 (2012).
12. Wu, P.-H. *et al.* A comparison of methods to assess cell mechanical properties. *Nature. Methods* **15**, 491–498 (2018).
13. Litvinov, R. I., Shuman, H., Bennett, J. S. & Weisel, J. W. Binding strength and activation state of single fibrinogen-integrin pairs on living cells. *Proc. Natl. Acad. Sci.* **99**, 7426–7431 (2002).
14. Bambardekar, K., Clément, R., Blanc, O., Chardès, C. & Lenne, P.-F. Direct laser manipulation reveals the mechanics of cell contacts in vivo. *Proc. Natl. Acad. Sci.* **112**, 1416–1421 (2015).
15. Guck, J. *et al.* The Optical Stretcher: A Novel Laser Tool to Micromanipulate Cells. *Biophys. J.* **81**, 767–784 (2001).
16. Scarcelli, G. & Yun, S. H. Confocal Brillouin microscopy for three-dimensional mechanical imaging. *Nature. Photonics* **2**, 39–43 (2008).
17. Scarcelli, G. *et al.* Noncontact three-dimensional mapping of intracellular hydromechanical properties by Brillouin microscopy. *Nature. Methods* **12**, 1132 (2015).
18. Prevedel, R., Diz-Muñoz, A., Ruocco, G. & Antonacci, G. Brillouin microscopy: An emerging tool for mechanobiology. *Nature. Methods* **16**, 969–977 (2019).
19. Brillouin, L. Diffusion de la lumière et des rayons X par un corps transparent homogène - Influence de l'agitation thermique. *Ann. Phys.* **9**, 88–122 (1922).
20. Boyd, R. W. *Nonlinear Optics* (Academic Press, 2008).
21. Scarcelli, G., Kim, P. & Yun, S. H. *In Vivo* Measurement of Age-Related Stiffening in the Crystalline Lens by Brillouin Optical Microscopy. *Biophys. J.* **101**, 1539–1545 (2011).
22. Antonacci, G. & Braakman, S. Biomechanics of subcellular structures by non-invasive Brillouin microscopy. *Sci. Reports* **6**, 37217 (2016).
23. Scarcelli, G., Pineda, R. & Yun, S. H. Brillouin Optical Microscopy for Corneal Biomechanics. *Investig. Ophthalmol. & Vis. Sci.* **53**, 185–190 (2012).
24. Antonacci, G., de Turris, V., Rosa, A. & Ruocco, G. Background-deflection Brillouin microscopy reveals altered biomechanics of intracellular stress granules by ALS protein FUS. *Commun. Biol.* **1**, 139 (2018).
25. Schlüßler, R. *et al.* Mechanical Mapping of Spinal Cord Growth and Repair in Living Zebrafish Larvae by Brillouin Imaging. *Biophys. J.* (2018).

26. Fiore, A. Direct Three-Dimensional Measurement of Refractive Index via Dual Photon-Phonon Scattering. *Phys. Rev. Lett.* **122** (2019).

27. Sung, Y. *et al.* Optical diffraction tomography for high resolution live cell imaging. *Opt. Express* **17**, 266–277 (2009).

28. Kim, K. *et al.* Optical diffraction tomography techniques for the study of cell pathophysiology. *J. Biomed. Photonics & Eng.* **2**, 020201 (2016).

29. Barer, R. Interference Microscopy and Mass Determination. *Nature.* **169**, 366–367 (1952).

30. Popescu, G. *et al.* Optical imaging of cell mass and growth dynamics. *Am. J. Physiol. - Cell Physiol.* **295**, C538–C544 (2008).

31. Zangle, T. A. & Teitell, M. A. Live-cell mass profiling: An emerging approach in quantitative biophysics. *Nat Meth* **11**, 1221–1228 (2014).

32. Zhao, H., Brown, P. H. & Schuck, P. On the Distribution of Protein Refractive Index Increments. *Biophys. J.* **100**, 2309–2317 (2011).

33. Theisen, A. *Refractive Increment Data-Book for Polymer and Biomolecular Scientists* (Nottingham University Press, Nottingham, 2000).

34. Erbe, A. & Sigel, R. Tilt angle of lipid acyl chains in unilamellar vesicles determined by ellipsometric light scattering. *The Eur. Phys. J. E, Soft Matter* **22**, 303–309 (2007).

35. Mashaghi, A., Swann, M., Popplewell, J., Textor, M. & Reimhult, E. Optical anisotropy of supported lipid structures probed by waveguide spectroscopy and its application to study of supported lipid bilayer formation kinetics. *Anal. Chem.* **80**, 3666–3676 (2008).

36. Alberti, S. & Dormann, D. Liquid–Liquid Phase Separation in Disease. *Annu. Rev. Genet.* **53**, 171–194 (2019).

37. Meichner, C. *et al.* Refractive-index determination of solids from first- and second-order critical diffraction angles of periodic surface patterns. *AIP Adv.* **5**, 087135 (2015).

38. Wang, C., Moyses, H. W. & Grier, D. G. Stimulus-responsive colloidal sensors with fast holographic readout. *Appl. Phys. Lett.* **107**, 051903 (2015).

39. Girardo, S. *et al.* Standardized microgel beads as elastic cell mechanical probes. *J. Mater. Chem. B* (2018).

40. Rahman, M. F. A., Arshad, M. R., Manaf, A. A. & Yaacob, M. I. H. An investigation on the behaviour of PDMS as a membrane material for underwater acoustic sensing. *IJMS Vol.41(6) [December 2012]* (2012).

41. Cafarelli, A. *et al.* Tuning acoustic and mechanical properties of materials for ultrasound phantoms and smart substrates for cell cultures. *Acta Biomater.* **49**, 368–378 (2017).

42. Brangwynne, C. P., Mitchison, T. J. & Hyman, A. A. Active liquid-like behavior of nucleoli determines their size and shape in Xenopus laevis oocytes. *Proc. Natl. Acad. Sci.* **108**, 4334–4339 (2011).

43. Schürmann, M., Scholze, J., Müller, P., Guck, J. & Chan, C. J. Cell nuclei have lower refractive index and mass density than cytoplasm. *J. Biophotonics* **9**, 1068–1076 (2016).

44. Kim, K. & Guck, J. The relative densities of cytoplasm and nuclear compartments are robust against strong perturbation. *Biophys. J.* (2020).

45. Lieberman, A. P., Shakkottai, V. G. & Albin, R. L. Polyglutamine Repeats in Neurodegenerative Diseases. *Annu. Rev. Pathol. Mech. Dis.* **14**, 1–27 (2019).

46. Norrbacka, S., Lindholm, D. & Myöhänen, T. T. Prolyl oligopeptidase inhibition reduces PolyQ aggregation and improves cell viability in cellular model of Huntington's disease. *J. Cell. Mol. Medicine* **23**, 8511–8515 (2019).

47. Bäuerlein, F. J. B. *et al.* In Situ Architecture and Cellular Interactions of PolyQ Inclusions. *Cell* **171**, 179–187.e10 (2017).

48. Yang, J. & Yang, X. Phase Transition of Huntingtin: Factors and Pathological Relevance. *Front. Genet.* **11** (2020).

49. Kroschwald, S. *et al.* Promiscuous interactions and protein disaggregases determine the material state of stress-inducible RNP granules. *eLife* **4**, e06807 (2015).

50. Patel, A. *et al.* A Liquid-to-Solid Phase Transition of the ALS Protein FUS Accelerated by Disease Mutation. *Cell* **162**, 1066–1077 (2015).

51. Alberti, S. & Hyman, A. A. Are aberrant phase transitions a driver of cellular aging? *BioEssays: News Rev. Mol. Cell. Dev. Biol.* **38**, 959–968 (2016).

52. Jawerth, L. M. Salt-Dependent Rheology and Surface Tension of Protein Condensates Using Optical Traps. *Phys. Rev. Lett.* **121** (2018).

53. Nötzel, M. *et al.* Axonal transport, phase-separated compartments and neuron mechanics — a new approach to investigate neurodegenerative diseases. *Front. Cell. Neurosci.* **12** (2018).

54. Brangwynne, C. P. *et al.* Germline P Granules Are Liquid Droplets That Localize by Controlled Dissolution/Condensation. *Sci.* **324**, 1729–1732 (2009).

55. Braet, F., Rotsch, C., Wisse, E. & Radmacher, M. Comparison of fixed and living liver endothelial cells by atomic force microscopy. *Appl. Phys. A* **66**, S575–S578 (1998).

56. Su, J.-W. *et al.* Investigation of influences of the paraformaldehyde fixation and paraffin embedding removal process on refractive indices and scattering properties of epithelial cells. *J. Biomed. Opt.* **19**, 075007 (2014).

57. Gouw, T. H. & Vlugter, J. C. Physical Properties of Triglycerides. I. Density and Refractive Index. *Fette, Seifen, Anstrichmittel* **68**, 544–549 (1966).

58. Liaw, L. *et al.* Lipid Profiling of In Vitro Cell Models of Adipogenic Differentiation: Relationships With Mouse Adipose Tissues. *J. Cell. Biochem.* **117**, 2182–2193 (2016).

59. Wabitsch, M. *et al.* Characterization of a human preadipocyte cell strain with high capacity for adipose differentiation. *Int. J. Obes.* **25**, 8–15 (2001).

60. Gouw, I. R. T. H. & Vlugter, I. R. J. C. Physical Properties of Triglycerides III: Ultrasonic Sound Velocity. *Fette, Seifen, Anstrichmittel* **69**, 159–164 (1967).

61. Caragine, C. M., Haley, S. C. & Zidovska, A. Nucleolar dynamics and interactions with nucleoplasm in living cells. *eLife* **8**, e47533 (2019).

62. Wu, P.-J. *et al.* Water content, not stiffness, dominates Brillouin spectroscopy measurements in hydrated materials. *Nature. Methods* **15**, 561–562 (2018).

63. Wu, P.-J. *et al.* Brillouin microscopy, what is it really measuring? *arXiv:1711.03312v2 [q-bio.QM]* (2018).

64. Scarcelli, G. & Yun, S. H. Reply to 'Water content, not stiffness, dominates Brillouin spectroscopy measurements in hydrated materials'. *Nature. Methods* **15**, 562–563 (2018).

65. Bailey, M. *et al.* Brillouin-derived viscoelastic parameters of hydrogel tissue models. *arXiv:1912.08292 [cond-mat, physics:physics]* (2019).

66. Oh, S. *et al.* In situ measurement of absolute concentrations by Normalized Raman Imaging. *bioRxiv* 629543 (2019).

67. Traverso, A. J. *et al.* Dual Raman-Brillouin Microscope for Chemical and Mechanical Characterization and Imaging. *Anal. Chem.* **87**, 7519–7523 (2015).

68. Abuhattum, S. *et al.* Intracellular Mass Density Increase Is Accompanying but Not Sufficient for Stiffening and Growth Arrest of Yeast Cells. *Front. Phys.* **6** (2018).

69. Scarcelli, G. & Yun, S. H. Multistage VIPA etalons for high-extinction parallel Brillouin spectroscopy. *Opt. Express* **19**, 10913–22 (2011).

70. Meng, Z., Traverso, A. J. & Yakovlev, V. V. Background clean-up in Brillouin microspectroscopy of scattering medium. *Opt. Express* **22**, 5410–5415 (2014).

71. Cuche, E., Marquet, P. & Depeursinge, C. Spatial filtering for zero-order and twin-image elimination in digital off-axis holography. *Appl. Opt.* **39**, 4070–4075 (2000).

72. Kim, K. *et al.* High-resolution three-dimensional imaging of red blood cells parasitized by *Plasmodium falciparum* and *in situ* hemozoin crystals using optical diffraction tomography. *J. Biomed. Opt.* **19**, 011005 (2014).

73. Müller, P., Schürmann, M. & Guck, J. The Theory of Diffraction Tomography. *arXiv:1507.00466 [physics, q-bio]* (2016).

74. Davies, H. G. & Wilkins, M. H. F. Interference Microscopy and Mass Determination. *Nature.* **169**, 541–541 (1952).

75. Fischer-Posovszky, P., Newell, F. S., Wabitsch, M. & Tornqvist, H. E. Human SGBS cells - a unique tool for studies of human fat cell biology. *Obes. Facts* **1**, 184–189 (2008).

Acknowledgements

We thank Anthony Hyman from the Max Planck Institute of Molecular Cell Biology and Genetics for providing the stable HeLa cell lines, Prof. Martin Wabitsch from the Centre for Hormonal Disorders in Children and Adolescents – Ulm University Hospital for providing the SGBS preadipocytes, and the Center for Molecular and Cellular Bioengineering Light Microscopy Facility (partly funded by the State of Saxony and the European Fund for Regional Development - EFRE) for technical support. Financial support from the Deutsche Forschungsgemeinschaft (SPP 2191 – Molecular mechanisms of functional phase separation, grant agreement number 419138906 to S.Al. and J.G.), Volkswagen Stiftung (grant agreement number 92847 to S.Al. and J.G.), the Alexander von Humboldt-Stiftung (Alexander von Humboldt-Professorship to J.G.) are gratefully acknowledged. A.H. is supported by the NOMIS foundation and the Hermann und Lilly Schilling-Stiftung für medizinische Forschung im Stifterverband.

Author contributions statement

R.S. evaluated the Brillouin measurements and wrote the software for the FOB microscope. K.K. evaluated the refractive index measurements. K.K. and R.S. realized the FOB microscope, conducted the FOB microscopy measurements and wrote the manuscript with contributions from all authors. M.N. and R.S. cultured the P525L HeLa cells, S.M. helped with HeLa polyQ transfection. S.G. produced the phantom beads. S.Ab. and A.T. prepared the adipocyte cells. G.C., T.B. and P.M. helped with the evaluation of the refractive index measurements. R.S., K.K., S.Al. and J.G. designed the experiments. All authors reviewed the manuscript.

Additional information

Accession codes The data sets generated during and/or analyzed during the current study are available from the corresponding author on reasonable request. **Competing financial interests** The authors declare no competing financial interests.